Premature jump-to-contact with elastic surfaces

Chuanli Yu, Zhaohe Dai *

Department of Mechanics and Engineering Science, State Key Laboratory for Turbulence and Complex Systems, College of Engineering, Peking University, Beijing 100871, China

ARTICLE INFO

ABSTRACT

Jump-to-contact is a commonly observed phenomenon in atomic force microscopy (AFM) measurements. It occurs when the AFM tip approaches the surface of the substrate, and the attractive forces – such as van der Waals forces – between the tip and the surface become sufficiently strong, causing the tip to jump towards the surface suddenly. Here, we investigate how the surface deformation affects the onset of jump-to-contact, and show that jump-to-contact happens prematurely in the deformable case (compared to the rigid case). We formulate this problem for surfaces that respond to external forces linearly and consider both retarded and non-retarded van der Waals forces. The jump-to-contact is investigated with linearly elastic substrates of arbitrary thicknesses. Specifically, we focus on small surface deformation relative to the tip–surface gap and perform a perturbation analysis for thin and thick substrates. Analytical solutions are obtained for the force or distance at which the jump occurs. These results should be useful for characterizing the strength and retardation behavior of van der Waals forces in soft materials and structures.

1. Introduction

Van der Waals (vdW) forces between atoms or molecules are universal; their importance has been recognized in a wide range of disciplines, including physics, mechanics, electronics, chemical engineering, materials science, and even biology (French et al., 2010). Just as noted by Feynman (1959) in his renowned lecture, *there's Plenty of Room at the Bottom*:"... As we go down in size, there are a number of interesting problems that arise... There is the problem that materials stick together by the molecular (van der Waals) attractions". This recognition has been accompanied by extensive efforts in the past century to precisely characterize the strength and behavior of vdW forces (Israelachvili, 2011), particularly by examining how two separate objects stick as they approach one another, or conversely, how two adhered objects are separated.

One of the first experiments on vdW force measurements was conducted by Tomlinson (1928), who used quartz fibers with radii of 6 µm as both testing materials and force sensors. At that time, there were diverse opinions on the decay of attractive molecular force F with distance d (Jones, 1924). Although a power law of the form $F \propto d^{-n}$ was proposed, the value of the exponent n was a subject of debate, with suggestions ranging from 2 to 8. Tomlinson (1928) observed that microfibers adhere quite *suddenly* as they approach each other, a phenomenon now known as pull-in, limit-point instability, or jump-to-contact in different fields, which is essentially caused by a saddle–node (fold) bifurcation (Gomez et al., 2017). He then measured the force required to pull off the fibers after jump-to-contact occurred. Bradley (1932) later improved Tomlinson's method by focusing on the separation of two unequal spheres. After the development of a satisfactory theory for dispersion force by London (1937) and the inclusion of retardation effects by Casimir (1948), it became well-established that $n = 6$ for ordinary, non-retarded vdW forces, and $n = 7$

---

for retarded vdW forces (Hamaker, 1937; Lifshitz, 1956). However, the pull-off forces measured in the experiments by Tomlinson (1928) and Bradley (1932) primarily reflect the strength of vdW forces or the surface energy of the solids. To reveal the long-range characteristics of vdW forces, it is necessary to measure the attractive pull-in forces between two solid bodies separated by a small gap.

Experiments of such type have been carried out since the 1950s (Derjaguin et al., 1956; Tabor and Winterton, 1969; Rouweler and Overbeek, 1971; Israelachvili and Tabor, 1972). The experimental setup typically involved a rigid glass hemisphere with highly polished surface. The force was determined by measuring the deflection of a cantilever to which the hemisphere was attached, and the gap between the surfaces was measured using optical interference techniques. In this way, the van der Waals forces between different types of glass were measured over a gap range of 25 to 1200 nm, and the existence of retardation effect was successfully confirmed (Derjaguin et al., 1956; Rouweler and Overbeek, 1971). Measuring ordinary, non-retarded van der Waals forces presented a greater challenge due to their presence only at very small separations. To address this, Tabor and Winterton (1969) exploited the critical distance at which two surfaces jump to contact, i.e., the phenomenon observed in earlier fiber experiments by Tomlinson (1928). This distance, which depends on the cantilever's stiffness, allowed for the first direct measurement of non-retarded vdW forces at separations below 10 nm, simply by employing cantilevers with varying stiffnesses (Tabor and Winterton, 1969; Israelachvili and Tabor, 1972). To date, advancements continue to be made in the precise measurement of both retarded and non-retarded vdW forces between different materials, utilizing cutting-edge techniques such as compact integrated silicon chips (Tang et al., 2017).

Over the past few decades, there has been a surge of remarkable advances in soft materials, slender structures, and nanomaterials. Today, the mechanical and surface properties of these materials are routinely explored using atomic force microscopy (AFM) (García and Perez, 2002), a technique that shares conceptual similarities with the static and dynamic experimental setups described by Tabor and Winterton (1969) and Israelachvili and Tabor (1972). Also, much like the jump-to-contact phenomenon used for vdW force measurements, AFM tips often abruptly adhere to the material being tested (Butt et al., 2005). This instability phenomenon is more pronounced in AFM measurements of soft materials and structures (Rutland et al., 2004; Dai et al., 2019, 2020), which can deform under vdW forces, thereby narrowing the gap between the tip and the surface and further enhancing the vdW interactions (Roberts, 1971). Analytical solutions for determining the critical jump-to-contact force or distance in these systems are very useful but challenging to obtain due to the complex, nonlinear interplay of vdW forces and elastic deformations. So far, only a few studies have addressed this problem (Greenwood, 1997; Feng, 2000; Wu, 2010; Ciavarella et al., 2017), and those that have often implicitly assume an infinitely stiff cantilever and rely heavily on numerical calculations with the consideration of additional repulsive vdW forces though they do not significantly influence the jump-to-contact. As a consequence, a deterministic understanding of the critical force and displacement at which the jump-to-contact occurs on deformable surfaces remains elusive, despite the widespread occurrence of this phenomenon in AFM measurements.

The objective of this work is to seek analytical solutions that can be directly applied to interpreting jump-to-contact force curves in AFM measurements of deformable materials. We achieve this by focusing on small surface deformations relative to the tip–surface gap and applying perturbation analysis to linearize the problem. Our approach is demonstrated for linearly elastic substrates, while we believe that it can be extended to other linear systems, such as liquid surfaces, plates, shells, and stretched membranes. The results may find immediate uses for characterizing the strength and retardation behavior of van der Waals forces in soft materials and structures. The paper is organized as follows. In Section 2, we formulate the problem for surfaces that respond to external forces linearly and discuss both retarded and non-retarded van der Waals forces. The focus of Section 3 is on linearly elastic substrates and non-retarded vdW forces. Analytical solutions are obtained for the critical jump force or distance, in the limit of small and large substrate thickness. Using a similar method, we address the retarded vdW forces (or, more generally, power-law long-range forces) in Section 4. Finally, in Section 5, we conclude with a summary of the main findings and their implications for characterizing the strength and retardation behavior of van der Waals forces in soft materials and structures.

2. Model

2.1. Equilibrium

We begin by discussing equilibrium equations in this nonlinear problem. Consider an AFM cantilever with an elastic stiffness k (Fig. 1). One end of the cantilever is fixed to a holder, while the other end is equipped with a spherical probe or tip of radius R_s. The height d of the holder above the undeformed surface is given by the sum of the cantilever deflection δ, the height of the probe s, and a reference distance d_{ref}:

$$d = \delta + s + d_{\text{ref}}, \tag{1}$$

In the following discussion, we will disregard the reference distance, focusing instead on the relative d for surfaces with varying degrees of deformability.

The interaction between the probe and the substrate is transduced into changes in the cantilever deflection, which can be detected experimentally. We then have

$$F = k\delta. \tag{2}$$

Alternatively, this interaction force can be analyzed by integrating the probe-substrate interaction across the entire domain:

$$F = \int_{\mathbb{R}^2} p_{\text{vdW}}(\boldsymbol{r}) \, \mathrm{d}^2 \boldsymbol{r}, \tag{3}$$
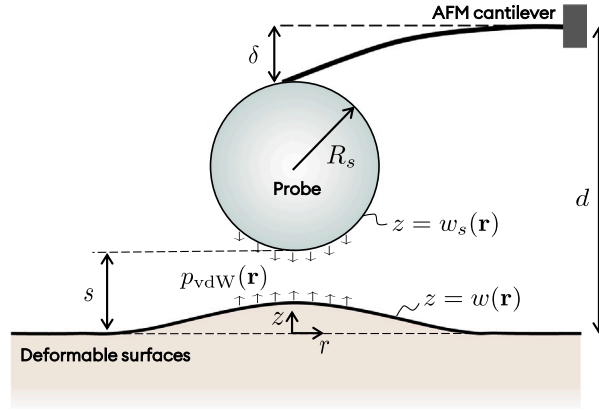
Fig. 1. Jump-in-contact on deformable surfaces. Consider an AFM tip of radius R_s mounted on a cantilever of spring constant k. The AFM tip interacts with the surface due to the attractive van der Waals forces. The height of the holder of the AFM cantilever above the undeformed surface is d and the height of the deflected tip is s.

where p_{vdW} is the attractive van der Waals forces per unit area between the two surfaces. The magnitude of p_{vdW} is a function of the gap $g(\boldsymbol{r})$ between the probe and the deformed substrate, defined as

$$g(\boldsymbol{r}) = w_s(\boldsymbol{r}) - w(\boldsymbol{r}), \tag{4}$$

where $w(\boldsymbol{r})$ is the surface deformation of the substrate, and $w_s(\boldsymbol{r})$ is the profile of the probe.

In calculating such net force around the point of minimum separation with $R_s \gg s$, it is typical to approximate spherical objects using a parabolic model (which is also part of the Derjaguin approximation, Derjaguin, 1934):

$$w_s(\boldsymbol{r}) \approx s + \frac{|\boldsymbol{r}|^2}{2R_s}. \tag{5}$$

The surface deformation field, $w(\boldsymbol{r})$ defined such that positive w closes the gap, arises due to the attractive vdW forces acting on the elastic surface. Shear stresses are considered negligible given the low viscosity of air (Dai and Vella, 2022). For linearly elastic materials and structures, the vdW forces and the surface deformation are typically related by

$$w(\boldsymbol{r}) = \int_{\mathbb{R}^2} p_{\mathrm{vdW}}(\boldsymbol{x}) G(\boldsymbol{r} - \boldsymbol{x}) \, \mathrm{d}^2 \boldsymbol{x}, \tag{6}$$

where $G(\boldsymbol{r} - \boldsymbol{x})$ represents the point response (Green) function that describes the deformation at $\boldsymbol{r}$ due to a normal point force applied at $\boldsymbol{x}$ (Rallabandi, 2024). The function G depends on the properties and geometry of the solid, and a comprehensive summary of boundary value problems involving linear partial differential equations for various types of elastic solids and structures can be found in Polyanin (2001).

2.2. Van der Waals interactions

The problem is to be complete with a specific relation for vdW forces between the sphere and the substrate. This relation has been extensively discussed in the literature (Israelachvili, 2011; Maugis, 2013). Briefly, the vdW interaction energy U between two molecules or atoms is given by

$$U_0 = -C/z^n, \tag{7}$$

where C is a constant representing the strength of such interaction, z is the distance between the molecules or atoms, and the exponent n is 6 for London dispersion (i.e., non-retarded) interactions (London, 1937) and is 7 for retarded interactions (Casimir and Polder, 1948). Assuming that vdW forces are additive, Hamaker (1937) demonstrated by integrating U_0 over the relevant domain that the interaction energy per unit area between two parallel surfaces separated by a uniform gap g is

$$U(g) = \begin{cases} -A/(2g^2), & \text{(Non-retarded)} \\ -B/(3g^3), & \text{(Retarded)} \end{cases} \tag{8}$$

where A and B are Hamaker constants for London and Casimir forces, respectively. Specifically, $A = \frac{\pi}{6} n_1 n_2 C$ and $B = \frac{\pi}{10} n_1 n_2 C$, with n_1 and n_2 denoting the number density of molecules or atoms in solid 1 and 2, respectively. Note that we have included the retarded case here and slightly modified the coefficients for notational convenience. The attractive forces between two parallel surfaces per unit area can then be calculated by $p_{\mathrm{vdW}} = \mathrm{d}U/\mathrm{d}g$, leading to

$$p_{\mathrm{vdW}} = \begin{cases} A/g^3, & \text{(Non-retarded)} \\ B/g^4. & \text{(Retarded)} \end{cases} \tag{9}$$
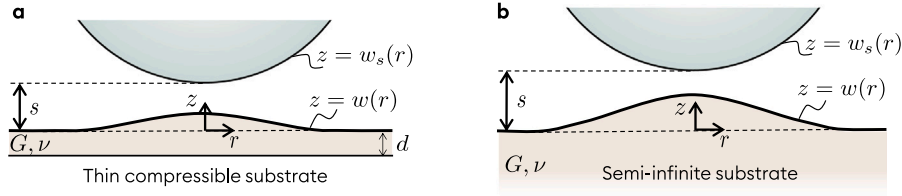
Fig. 2. Schematic illustration and notation of the elastic substrate experiencing transverse attractive vdW forces from a spherical tip. The analysis focuses on two limiting cases: (a) thin substrates and (b) thick substrates.

To calculate the interaction between a sphere and a slightly deformed surface, we can replace g in Eq. (9) with $g(r)$ given in Eq. (4), following the Derjaguin approximation. This approach is reasonable as long as $R_s \gg s$ and the "rotation" of the deformed surface is moderate ($w'^2 \ll 1$).

2.3. Linearly elastic substrates

The problem outlined above can be applied to interpret AFM force curves measured on nanoflakes (Wang et al., 2019), cell membranes (Krieg et al., 2019; Guimarães et al., 2020), pre-stretched elastic sheets (Dai and Lu, 2021; Rao and Lu, 2024), and even liquid surfaces (Costa et al., 2017), simply by adopting the corresponding Green's function for their mechanical response (Polyanin, 2001). However, this work specifically focuses on the scenario of linearly elastic substrates with finite thicknesses (Fig. 2), which are prevalent in a range of nature and engineering systems (Style and Dufresne, 2012; Dillard et al., 2018; Bertin et al., 2022; Fang et al., 2022). In this context, the problem is axisymmetric and most conveniently solved by transforming it into the Hankel domain (Sneddon, 1995):

$$\tilde{f}(\xi) = \mathcal{H}_0[f(r)] = \int_0^\infty f(r) J_0(\xi r) r \, dr, \tag{10}$$

with the inverse transform given by

$$f(r) = \mathcal{H}_0^{-1}[\tilde{f}(\xi)] = \int_0^\infty \tilde{f}(\xi) J_0(\xi r) \xi \, d\xi. \tag{11}$$

Specifically, the linearly elastic response of the substrate in the Hankel domain is given by

$$\tilde{w}(\xi) = \mathcal{K}(\xi) \tilde{p}_{vdW}(\xi), \tag{12}$$

where the kernel function is

$$\mathcal{K}(\xi) = \frac{1-\nu}{G\xi} \times \frac{(3-4\nu)\sinh(2\xi t) + 2\xi t}{(3-4\nu)\cosh(2\xi t) + 2(\xi t)^2 + 5 - 12\nu + 8\nu^2}, \tag{13}$$

as described by Hannah (1951), where G is shear modulus and ν is Poisson's ratio of the substrate material. The surface deformation due to vdW forces can then be calculated as

$$w(r) = \mathcal{H}_0^{-1}\left[\mathcal{K}(\xi)\mathcal{H}_0\left[p_{vdW}(r)\right]\right]. \tag{14}$$

3. Non-retarded vdW forces

3.1. Rigid substrate

In this section, we investigate the jump-to-contact phenomenon using non-retarded vdW forces. We begin by reviewing the force curves and length scales in the system of rigid substrates (as discussed in Tabor and Winterton, 1969). In this case, $w = 0$ and substituting Eqs. (4) and (9) into Eq. (3) yields

$$F = \pi A R_s / s^2, \tag{15}$$

which was first derived by Hamaker (1937). Tabor and Winterton (1969) considered the effect of flexible cantilevers, to show which one can use Eqs. (1), (2), and (15) to have

$$d = s + \frac{\pi A R_s}{k s^2}. \tag{16}$$

To illustrate the jump-to-contact instability, we can plot the gap s between the sphere tip and rigid surface, as well as the force F required to pull the sphere against vdW attraction, as functions of the relative height d of the cantilever holder, as schematically shown in Fig. 1. The righthand side of Eq. (16) immediately suggests a characteristic length scale:

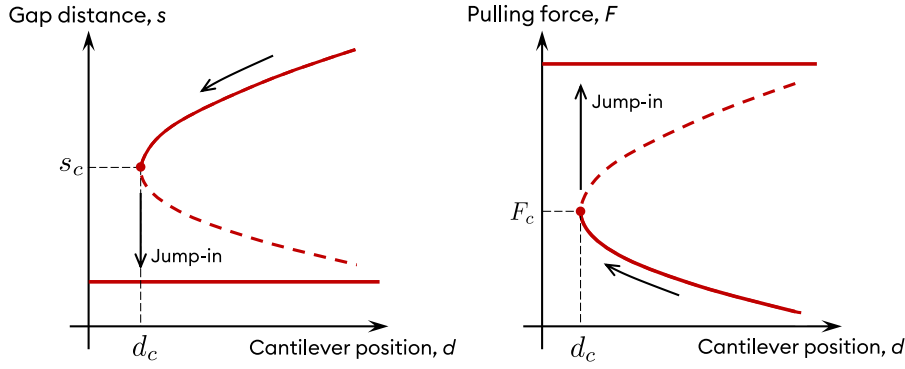$$s_* := (A R_s / k)^{1/3}, \tag{17}$$

Fig. 3. Schematic illustration of the jump-to-contact as saddle–node bifurcation. (a) The gap s between the sphere tip and the substrate surface as a function of the position d of the cantilever holder. Given a sufficiently large d, the problem has two solutions (denoted by the solid and dashed curves), while the solution corresponding to the larger gap (i.e., the solid curve) is stable. The arrows indicate the process of moving the sphere from a stale state towards the substrate surface. The jump-to-contact instability occurs at $d = d_c$ (at that moment $s = s_c$); Subsequently, the gap reduces to a specific value (indicated by the horizontal solid line), determined by the balance between attractive and repulsive van der Waals forces. (b) The force required to pull the sphere against vdW attraction as of the position of the cantilever holder. Again, the solid and dashed curves denote stable and unstable solutions, respectively, and the arrows illustrate the approaching process.

which can be adjusted by using spheres of different radii and cantilevers with varying stiffness. Experimentally, this length scale can range from a few nanometers to several microns (Israelachvili and Tabor, 1972).

When the cantilever is positioned sufficiently far from the substrate surface ($d \gtrsim s_*$), Eq. (16) yields two solutions for the gap and force, as represented by the solid and dashed curves in Fig. 1. Only the solution corresponding to the larger gap or smaller pulling force (i.e., the solid curves in Fig. 1) is stable to perturbations. If the system starts in this stable equilibrium state, gradually moving the cantilever downward brings the sphere closer to the substrate. The stable state (solid curve) eventually disappears at the point (d_c, s_c) and (d_c, F_c) in Fig. 3, where it merges with the unstable state. Beyond this point, the sphere abruptly jumps into contact with the substrate, causing the gap to close and the pulling force to blow up. This transition corresponds to a saddle–node (fold) bifurcation or limit-point instability, where the current equilibrium state suddenly ceases to exist (Liu et al., 2021). Notably, in practice, the gap does not fully close after the jump-to-contact, and the pulling force does not become infinite. Calculating the gap and pulling force after contact requires accounting for repulsive vdW forces and specific adhesion mechanics theories (see Greenwood, 1997), which are beyond the scope of this study. Instead, our primary interest is in the critical cantilever position d_c, the critical sphere position s_c, and the critical pulling force F_c at the onset of the bifurcation, particularly how they depend on the deformability of the substrate.

Before discussing elastic substrates, we introduce the horizontal characteristic length of this system following the typical concept of contact mechanics (Ciavarella et al., 2019):

$$\ell_* := (R_s s_*)^{1/2} = A^{1/6} R_s^{2/3} / k^{1/6}. \tag{18}$$

As the sphere approaches an elastic substrate, we expect the substrate to deform by a certain amount w_* (to be discussed) over the region characterized by $r \lesssim \ell_*$. The purpose of introducing such horizontal length is to define the effective thickness of the substrate or the inverse of the slenderness ratio by

$$\mathcal{T} := \frac{t}{\ell_*} = \frac{k^{1/6} t}{A^{1/6} R_s^{2/3}}, \tag{19}$$

where t is the thickness of the substrate (Fig. 2a). We will simplify the analysis for very thin substrates ($\mathcal{T} \ll 1$) and very thick substrates ($\mathcal{T} \gg 1$) to seek analytical insights that have previously been elusive. Specifically, the kernel function in Eq. (13) can be largely simplified (Li et al., 2024):

$$\mathcal{K}(\xi) = \frac{1}{G} \begin{cases} \frac{(1-2\nu)}{2(1-\nu)} t + \frac{\nu(4\nu-1)}{6(1-\nu)^2} \xi^2 t^3, & \text{as} \quad \mathcal{T} \ll 1, \\ (1-\nu)/|\xi|, & \text{as} \quad \mathcal{T} \gg 1. \end{cases} \tag{20}$$

3.2. Thin compressible substrate

In addition to the parameter $\mathcal{T}$, which characterizes the effective thickness of the substrate, there are other dimensionless parameters, including at least one that defines the effective deformability of the substrate (i.e., the reverse of the effective stiffness of the substrate). To elucidate this parameter, we first consider the case of thin elastic substrates (Fig. 2a).

In the limit of thin substrates, Eq. (20) suggests that the substrate behaves like an array of independent elastic spring of stiffness $\sim G/t$, as long as its Poisson's ratio is not too close to $1/2$. Let us consider the case of a compressible substrate with relatively small

deformation so that the typical pressure due to non-retarded vdW forces is given by $p_* \sim A/s_*^3$, according to Eq. (9). The typical deformation of the substrate surface can then be estimated as

$$w_* \sim p_* t/G \sim (1 - 2v)tA/[2(1 - v)Gs_*^3]. \tag{21}$$

We then compare this vdW attraction induced substrate deformation to the characteristic jump-in gap s_*, leading to

$$\epsilon_c := \frac{(1 - 2v)tA}{2(1 - v)Gs_*^4} = \frac{(1 - 2v)tk^{4/3}}{2(1 - v)GA^{1/3}R_s^{4/3}}. \tag{22}$$

We note that the subscript c in ϵ_c denotes 'compressible' throughout the main text, whereas in the critical parameters associated with the onset of jump-to-contact, such as s_c, F_c, and d_c, it represents 'critical'. Clearly, ϵ_c provides a measure of the deformability of the substrate: a system with a small ϵ_c corresponds to relatively stiff substrates, and vice versa.

3.2.1. Non-dimensionalization

We use s_* in Eq. (17) as the vertical length and ℓ_* in Eq. (18) as the horizontal length to rescale the variables:

$$\rho = r/\ell_*, \quad X = \xi\ell_*, \quad W = w/s_*, \quad W_s = w_s/s_*, \quad P = p_{\text{vdW}}s_*^3/A, \quad \tilde{P} = \tilde{p}_{\text{vdW}}s_*^3/(A\ell_*^2)$$
$$S = s/s_*, \quad D = d/s_*, \quad \mathcal{F} = Fs_*^2/(AR_s) \tag{23}$$

The dimensionless problem now involves a sphere with an approximate profile:

$$W_s(\rho) = S + \frac{1}{2}\rho^2 \tag{24}$$

subject to vdW attraction from the elastic substrate:

$$P(\rho) = 1/(W_s - W)^3, \tag{25}$$

in which the substrate deformation is calculated by

$$W(\rho) = \epsilon_c \int_0^\infty \tilde{\mathcal{K}}_c(X) \left(\int_0^\infty P(\rho)J_0(X\rho)\rho \, d\rho \right) J_0(X\rho)X \, dX, \tag{26}$$

or simply $W = \epsilon_c \mathcal{H}_0^{-1}[\tilde{\mathcal{K}}_c(X)\tilde{P}(X)]$, where

$$\tilde{\mathcal{K}}_c(X) = \frac{2(1 - v)^2}{1 - 2v} \frac{(3 - 4v)\sinh(2\mathcal{T}X) - 2\mathcal{T}X}{\mathcal{T}X\left[(3 - 4v)\cosh(2\mathcal{T}X) + 2(\mathcal{T}X)^2 + 5 - 12v + 8v^2\right]}. \tag{27}$$

The total attractive vdW forces can be calculated by

$$\mathcal{F} = 2\pi \int_0^\infty P\rho \, d\rho, \tag{28}$$

and finally the geometry requires

$$D = S + \mathcal{F}. \tag{29}$$

Interestingly, such non-dimensionalization suggests that v, $\mathcal{T}$, and ϵ_c are the only three dimensionless parameters in the problem. Note that while we have implied $\mathcal{T} \ll 1$ and $\epsilon_c \ll 1$ to reach the form in Eq. (22), our calculations of the problem specified in Eqs. (24) to (29) can be carried out for any values of $\mathcal{T}$ and ϵ_c.

It is also worth noting that AFM experiments typically control the position of the cantilever holder, D, and measure the pulling force, $\mathcal{F}$, experienced by the sphere or cantilever. Alternatively, though less commonly, the holder displacement is varied in order to reach a prescribed pulling (sometimes pushing) force. In numerical calculations, however, it is more straightforward to prescribe the separating distance of the sphere, S, and then calculate the corresponding force, $\mathcal{F}$, and the cantilever position, D, required to achieve this separation.

We present numerically calculated $S - D$ and $\mathcal{F} - D$ relations for $\mathcal{T} = 0.01$, $v = 0.3$, and various values of ϵ_c, as indicated by the '+' markers in Fig. 4. The saddle–node bifurcation structure observed in the limit of rigid substrates (Fig. 1) is reproduced. We find that as ϵ_c decreases (i.e., as the effective stiffness increases), the numerical results converge to those of a rigid substrate (i.e., black curves in Fig. 4). As expected, with increasing substrate deformability (ϵ_c), the jump-to-contact occurs earlier: at a larger cantilever position, with a greater gap between the sphere tip and undeformed substrate, and thus at smaller pulling forces. This premature bifurcation can be readily understood, as substrate deformation narrows the gap between the sphere and the substrate and enhances their van der Waals attraction.

Note that typical AFM measurements may be used to plot the negative pulling force $(-\mathcal{F})$ as a function of the tip–substrate distance (S), as illustrated in Fig. 5. For rigid substrates, fitting such data with $\mathcal{F} = \pi/S^2$ allows for the evaluation of the additivity and retardation effects of vdW interactions between the sphere and the substrate (see Figure 13.6 in Israelachvili, 2011). Our results indicate that for deformable substrates, their deformation can 'alter' the exponent in the power-law relationship between $\mathcal{F}$ and S, particularly when ϵ_c is not small.
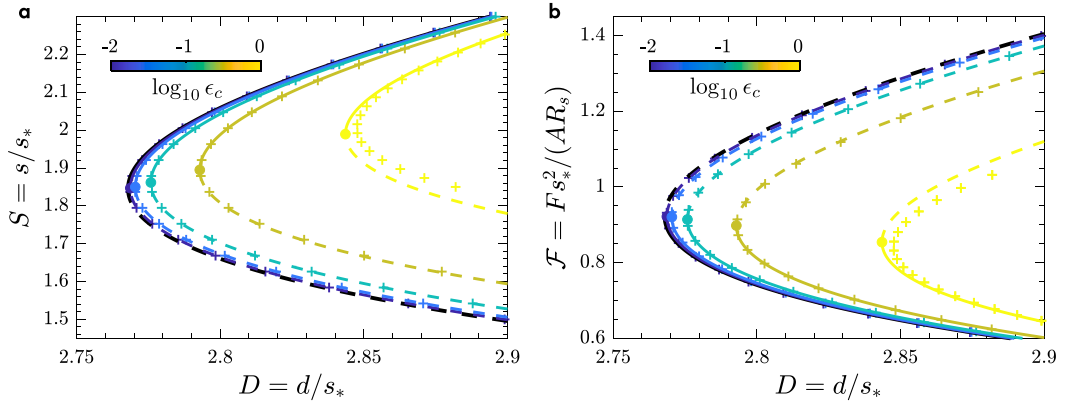
Fig. 4. The jump-to-contact on thin compressible substrates. (a) The dimensionless distance of the sphere tip above the undeformed substrate S as a function of the dimensionless position D of the cantilever holder. (b) The dimensionless pulling forces $\mathcal{F}$ as a function of the dimensionless position D of the cantilever holder. All curves represent analytical solutions given by (35) and (36), obtained under the condition $\mathcal{T} \ll 1$ and $\epsilon_c \ll 1$. The '+' markers represent numerical calculations based on $\mathcal{T} = 0.01$ and $\nu = 0.3$. Curves and makers of the same color correspond to the same ϵ_c values, as encoded in the associated color bar. The filled circle markers at which the solid (stable state) and dashed (unstable state) curves meet denote the bifurcation points. The black dashed and solid curves represent the case of a rigid substrate.
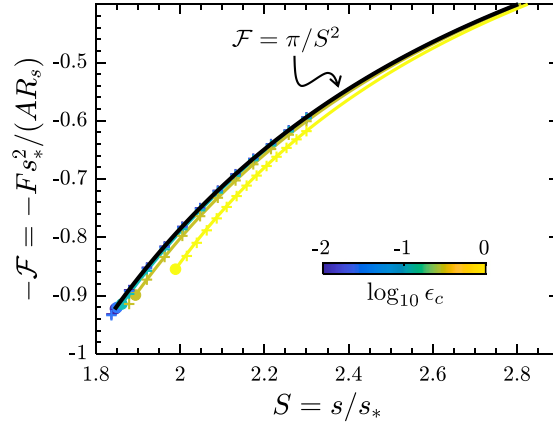

Fig. 5. Negative pulling force as a function of the gap between the sphere and undeformed substrate, just before the onset of jump-to-contact. The dashed and solid curves, along with the markers, are all reproduced from Fig. 4. The black solid curve represents the case of rigid substrate in which $\mathcal{F} = \pi/S^2$.

3.2.2. Perturbation theory

To gain more quantitative insights into the premature jump-to-contact, we seek analytical solutions at small ϵ_c and $\mathcal{T}$. Particularly, the use of thin compressible substrates allows us to simplify Eq. (27) as:

$$\tilde{\mathcal{K}}_c \to 1 \quad \text{as} \quad \mathcal{T} \ll 1 \tag{30}$$

at the leading order $O(\mathcal{T}^0)$. We will discuss what is meant by compressible for a thin substrate shortly. In this regime, the elastic response of the thin substrate, i.e., Eq. (26), simply becomes

$$W(\rho) = \epsilon_c P(\rho). \tag{31}$$

We then consider a relatively stiff substrate ($\epsilon_c \ll 1$) and perform a perturbation analysis as follows:

$$W(\rho) = W_0(\rho) + \epsilon_c W_1(\rho) + \epsilon_c^2 W_2(\rho) + O(\epsilon_c^3)$$
$$P(\rho) = P_0(\rho) + \epsilon_c P_1(\rho) + \epsilon_c^2 P_2(\rho) + O(\epsilon_c^3), \tag{32}$$

where the subscript 0 indeed corresponds to the solution for a rigid substrate. This can be easily seen by plugging Eq. (32) into Eq. (31):

$$W_0 + \epsilon_c(W_1 - P_0) + \epsilon_c^2(W_2 - P_1) + \cdots = 0, \tag{33}$$
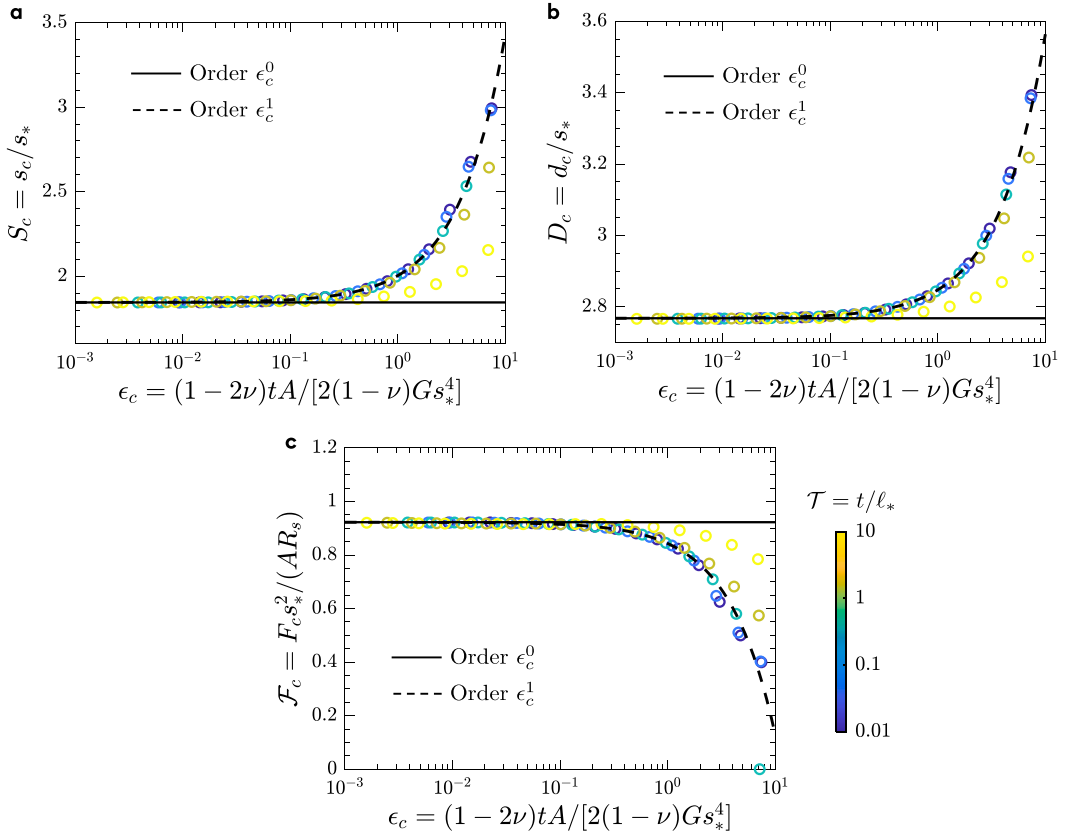
Fig. 6. Onset of jump-to-contact on thin compressible substrates. (a) The critical gap S_c between the sphere and the undeformed substrate (see notation in Fig. 2a) as a function of the effective deformability of the substrate ϵ_c defined in Eq. (22). (b) The critical cantilever position D_c (see notation in Fig. 1) as a function of ϵ_c. (c) The critical pulling force $\mathcal{F}_c$ as a function of ϵ_c. The solid and dashed curves represent the zeroth- and first-order solution given in Eq. (37), respectively. The markers indicate numerical calculations for different effective substrate thickness $\mathcal{T}$, with the specific values corresponding to the colors shown in the color bar. Here, $\nu = 0.3$.

implying $W_0 = 0$ (zero substrate deformation). Given this and $\epsilon_c \ll 1$, we combine Eq. (32) and the nonlinear vdW forces in Eq. (25) to obtain

$$\left(P_0 - \frac{1}{W_s^3}\right) + \epsilon_c\left(P_1 - \frac{3W_1}{W_s^4}\right) + \epsilon_c^2\left(P_2 - \frac{6W_1^2}{W_s^5} - \frac{3W_2}{W_s^4}\right) + \cdots = 0 \tag{34}$$

We then obtain the zeroth-order (rigid-substrate) solution: $W_0 = 0$ and $P_0 = 1/W_s^3$, the first-order solution: $W_1 = 1/W_s^3$ and $P_0 = 3/W_s^7$, and the second-order solution: $W_2 = 3/W_s^7$ and $P_0 = 15/W_s^{11}$, and so on. Applied such results to Eqs. (28) and (29) gives rise to:

$$D = \left(S + \frac{\pi}{S^2}\right) + \frac{\pi}{S^6}\epsilon_c + \frac{3\pi}{S^{10}}\epsilon_c^2 + O(\epsilon_c^3) \tag{35}$$

and

$$\mathcal{F} = \frac{\pi}{S^2} + \frac{\pi}{S^6}\epsilon_c + \frac{3\pi}{S^{10}}\epsilon_c^2 + O(\epsilon_c^3). \tag{36}$$

The analytical $S - D$ and $F - D$ relations are also plotted in Fig. 4 (see colored curves), showing excellent agreement with numerical calculations even at $\epsilon_c \sim 1$. Moreover, based on Eqs. (35) and (36), the critical gap, cantilever position, and pulling force can be analytically expressed as:

$$S_c = (2\pi)^{1/3} + \frac{1}{2\pi}\epsilon_c, \quad D_c = \left(\frac{27\pi}{4}\right)^{1/3} + \frac{1}{4\pi}\epsilon_c, \quad \text{and} \quad \mathcal{F}_c = \left(\frac{\pi}{4}\right)^{1/3} - \frac{1}{4\pi}\epsilon_c. \tag{37}$$

The accuracy of Eq. (37) is anticipated to be on the order of ϵ_c^2. However, we extended Eqs. (32) to (36) to the 11th order in ϵ_c and found that the higher-order terms of ϵ_c have no impact on the jump-to-contact point. This suggests that Eq. (37) may remain accurate even for moderate ϵ_c (to be demonstrated in Fig. 6).

In Fig. 6, we compare the analytical solutions from Eq. (37) with numerical results calculated using $v = 0.3$ and various values of $\mathcal{T}$ and ϵ_c. While these analytical expressions are derived under the assumption that the substrate is sufficiently thin ($\mathcal{T} \ll 1$) and stiff ($\epsilon \ll 1$), we find that the first-order solutions perform surprisingly well even at $\epsilon_c \sim 10$ and $\mathcal{T} \sim 10$. A noticeable deviation between the analytical and numerical results only occurs for very large $\mathcal{T}$, where the simplified spring-like mechanical response in Eq. (31) no longer holds. We then proceed to consider the alternative limit, where the substrate is thick ($\mathcal{T} \gg 1$).

3.3. Semi-infinite substrate

In the limit of a semi-infinite substrate or half-space, we must introduce a different expression to characterize the substrate's effective deformability. We apply an energetic argument: the strain level ϵ is proportional to w_*/ℓ_* in a half-space and the elastic strain energy stored in the half-space scales as $G\epsilon^2 \times V$, where the typical volume $V \sim \ell_*^3$. This energy should be comparable to the work done by vdW forces, which scales as $p_* \ell_*^2 \times w_*$, with $p_* \sim A/s_*^3$. We then obtain the typical vertical deformation on the substrate surface: $w_* \sim p_* \ell_*/G$. By comparing this typical deformation to the characteristic jump-in gap s_*, we have

$$\epsilon_s := \frac{A\ell_*}{Gs_*^4} = \frac{k^{7/6}}{GA^{1/6}R_s^{2/3}} \tag{38}$$

to present the effective deformability of a semi-infinite space. Here, the subscript s in ϵ_s denotes 'semi-infinite'. Note that this differs from the effective deformability of a thin substrate by

$$\epsilon_c = \frac{1-2v}{2(1-v)}\mathcal{T}\epsilon_s. \tag{39}$$

We use the same non-dimensionalization as in Eq. (23), as it is based on a rigid substrate and is independent of substrate elasticity. The problem formulation remains as specified in Eqs. (23) to (29). However, for greater consistency, ϵ_c should be replaced with ϵ_s in Eq. (26), and the kernel in Eq. (26) should be modified to:

$$\tilde{\mathcal{K}}_s(X) = \frac{(1-v)\left[(3-4v)\sinh(2\mathcal{T}X) - 2\mathcal{T}X\right]}{X\left[(3-4v)\cosh(2\mathcal{T}X) + 2(\mathcal{T}X)^2 + 5 - 12v + 8v^2\right]}. \tag{40}$$

The dimensionless parameters in this problem are exclusively v, $\mathcal{T}$, and ϵ_s. Using $v = 0.3$, we plot the numerical calculated $S - D$ and $\mathcal{F} - D$ relations (shown with '+' markers in Fig. 7a and b), as well as the critical cantilever position D_c and critical pulling force $\mathcal{F}_c$ (indicated by 'o' markers in Fig. 7c and d). The phenomenon of premature jump-to-contact is observed again as the substrate deformability increases (i.e., with increasing ϵ_s).

Using a similar method applied to the thin compressible substrate, we analyze the half-space problem with $\mathcal{T} \gg 1$. In this limit, the kernel function in Eq. (40) simplifies to:

$$\tilde{\mathcal{K}}_s \to (1-v)/|X|. \tag{41}$$

We can then proceed with the perturbation analysis (in the Hankel space) and obtain the following structure:

$$W_0 + \epsilon_s\left\{W_1 - (1-v)\mathcal{H}_0^{-1}\left[\tilde{P}_0/|X|\right]\right\} + \epsilon_s^2\left\{W_2 - (1-v)\mathcal{H}_0^{-1}\left[\tilde{P}_1/|X|\right]\right\} + \cdots = 0,$$

$$\left(P_0 - \frac{1}{W_s^3}\right) + \epsilon_s\left(P_1 - \frac{3W_1}{W_s^4}\right) + \epsilon_s^2\left(P_2 - \frac{6W_1^2}{W_s^5} - \frac{3W_2}{W_s^4}\right) + \cdots = 0. \tag{42}$$

The zeroth-order solution remains the rigid-substrate solution, while the first-order solution is found:

$$W_1(\rho) = \frac{(1-v)\left[2\left(4S+\rho^2\right)\text{E}\left(-\rho^2/2S\right) - \left(2S+\rho^2\right)\text{K}\left(-\rho^2/2S\right)\right]}{2\sqrt{2}\,S^{3/2}\left(2S+\rho^2\right)^2},$$

$$P_1(\rho) = \frac{12\sqrt{2}\,(1-v)\left[2\left(4S+\rho^2\right)\text{E}\left(-\rho^2/2S\right) - \left(2S+\rho^2\right)\text{K}\left(-\rho^2/2S\right)\right]}{S^{3/2}\left(2S+\rho^2\right)^6}, \tag{43}$$

where E and K are the complete elliptic integrals of the first and the second kinds (Abramowitz and Stegun, 1968).

Finally, we derive the analytical $S - D$ and $\mathcal{F} - D$ solution up to the first order:

$$D = \left(S + \frac{\pi}{S^2}\right) + \frac{2835\,\pi^3}{16384\sqrt{2}}\frac{1-v}{S^{11/2}}\epsilon_s + O(\epsilon_s^2) \quad \text{and} \quad \mathcal{F} = \frac{\pi}{S^2} + \frac{2835\,\pi^3}{16384\sqrt{2}}\frac{1-v}{S^{11/2}}\epsilon_s + O(\epsilon_s^2) \tag{44}$$

as well as the critical conditions at the onset of jump-to-contact, including:

$$S_c = (2\pi)^{1/3} + \frac{10395\,\pi^{7/6}}{131072 \times 2^{1/3}}(1-v)\epsilon_s \tag{45}$$

and

$$D_c = \left(\frac{27\pi}{4}\right)^{1/3} + \frac{2835\,\pi^{7/6}}{65536 \times 2^{1/3}}(1-v)\epsilon_s, \quad \mathcal{F}_c = \left(\frac{\pi}{4}\right)^{1/3} - \frac{4725\,\pi^{7/6}}{131072 \times 2^{1/3}}(1-v)\epsilon_s. \tag{46}$$

These analytical results are compared with numerics in Fig. 7. We find good agreement between them as long as $\epsilon_s \lesssim 1$ and $\mathcal{T} \gtrsim 10$. For example, the numerical results in Fig. 7c and d eventually converge to the solid (master) curve given by Eq. (46) as $\mathcal{T}$ increases.
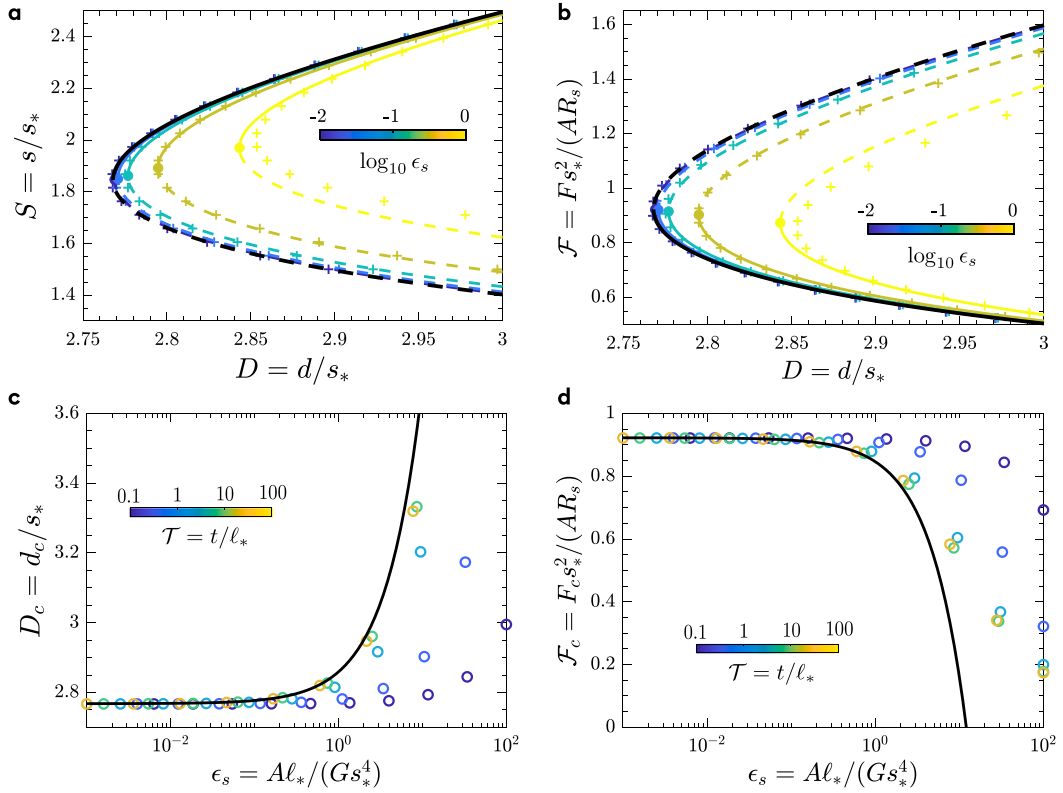
Fig. 7. The jump-to-contact on semi-infinite substrates. (a) The dimensionless distance of the sphere tip above the undeformed substrate S as a function of the dimensionless position D of the cantilever holder for various ϵ_s defined in Eq. (38). (b) The dimensionless pulling forces F as a function of the dimensionless position D of the cantilever holder. In (a) and (b), the black dashed and solid curves represent the case of a rigid substrate, and colored curves represent analytical solutions for various ϵ_s given in Eq. (44). The '+' markers denote numerical calculations based on $\mathcal{T} = 100$. (c) The critical cantilever position D_c (see notation in Fig. 1) as a function of ϵ_s. (d) The critical pulling force $\mathcal{F}_c$ as a function of ϵ_s. In (c) and (d), the solid curves represent the first-order solutions for thick substrates given in Eq. (46). The 'o' markers are numerical calculations for different values of ϵ_s and $\mathcal{T}$. In all panels, curves and makers of the same color correspond to the same parameter, as encoded in the associated color bar of each panel. Here, $v = 0.3$.

3.4. Thin incompressible substrates

Lastly, we discuss the particular case of a thin substrate of a Poisson's ratio very close to $1/2$. In this case, the substrate deformability ϵ_c approaches zero, according to Eq. (22). However, this is not entirely accurate, as the substrate can still deform via shear while conserving the total volume (see illustration in Fig. 8a). To resolve this inconsistency, we need to expand the kernel function in Eq. (20) up to $O(\mathcal{T}^2)$. By comparing the second and first terms of this expansion, we obtain a dimensionless parameter that can be used to characterize the material's effective compressibility:

$$C := (1 - 2v)\frac{\ell_*^2}{t^2} = (1 - 2v)\mathcal{T}^{-2} \tag{47}$$

This indicates that the effective compressibility of a thin substrate is governed not only by its Poisson ratio but also by its effective thickness. Such dependence on the geometrical slenderness is conceptually similar to the effective Reynolds number in lubrication theory (Tavakol et al., 2017) and was also reported by Chandler and Vella (2020) in the indentation and soft lubrication problem.

To characterize the deformability of a thin substrate with limited compressibility ($C \to 0$), we revisit the energetic argument discussed for a half-space: the strain energy, which scales as $G\epsilon^2 \times V$, should be comparable to the work done by the vdW forces $\sim p_*\ell_*^2 \times w_*$. For a thin substrate, the typical volume V is given by $t\ell_*^2$. The magnitude of strain requires careful consideration. The incompressibility or volume conservation condition implies that the horizontal displacement u_* satisfies $u_*/\ell_* \sim w_*/t$. The relevant strain here is the shear strain, which scales as $u_*/t \sim w_*\ell_*/t^2$. Thus, we have $w_* \sim p_*t^3/(G\ell_*^2)$. Comparing this to the characteristic gap size s_*, we obtain the effective deformability of a thin incompressible substrate:

$$\epsilon_i := \frac{t^3 A}{G R_s s_*^5} = \frac{t^3 k^{5/3}}{G A^{2/3} R_s^{8/3}}, \tag{48}$$

which is related to the deformability of a thin compressible substrate via

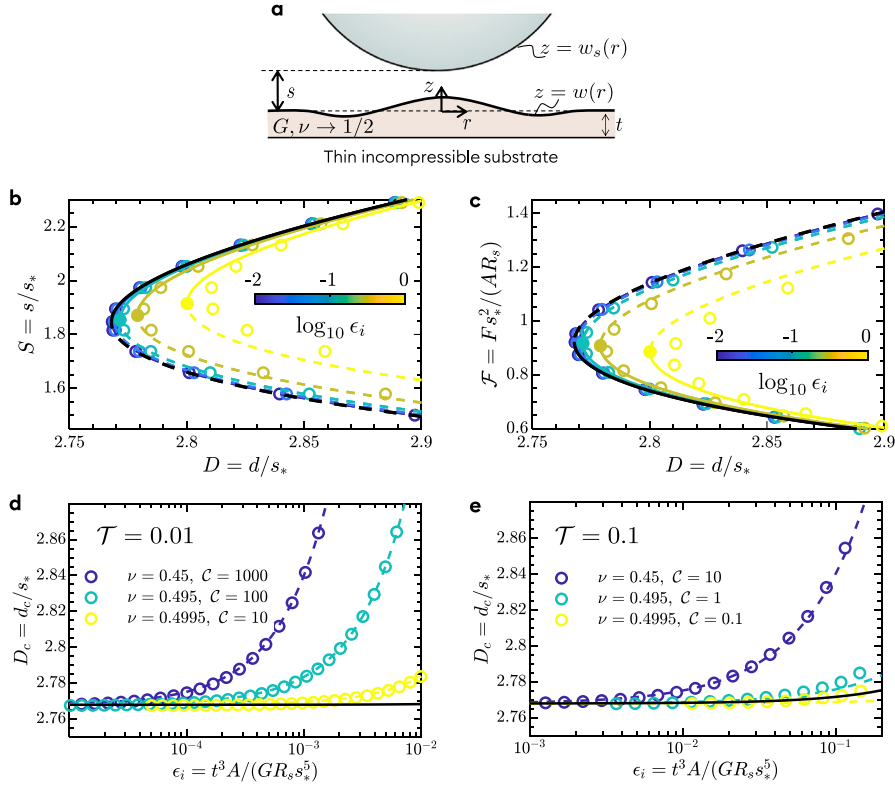$$\epsilon_c = \frac{C}{2(1 - v)}\epsilon_i. \tag{49}$$

Fig. 8. The jump-to-contact on thin incompressible substrates. (a) Schematic illustration and notation of a thin incompressible elastic substrate experiencing attractive vdW forces from a spherical tip. The dimensionless gap of the sphere tip above the undeformed substrate S (b) and the dimensionless pulling force $\mathcal{F}$ (c) as functions of the dimensionless position D of the cantilever holder for various ϵ_s defined in Eq. (48). The black dashed and solid curves represent the case of a rigid substrate, and colored curves represent analytical solutions for various ϵ_s given in Eq. (53). The 'o' markers represent numerical calculations based on $\mathcal{T} = 0.01$ and $\nu = 0.5$. The critical cantilever position D_c as a function of ϵ_i for various Poisson's ratios with $\mathcal{T} = 0.01$ (d) and $\mathcal{T} = 0.1$ (e). The solid and dashed curves represent the first-order solutions for thin incompressible substrates given in Eq. (54) and thin compressible substrates given in Eq. (37), respectively. The 'o' markers are numerical calculations for different values of ϵ_i and ν.

Here, the subscript i in ϵ_i stands for 'incompressible'.

We continue to follow the problem formulation given in Eqs. (23) to (29) but we replace ϵ_c with ϵ_i in Eq. (26) and modify the kernel function in Eq. (26) to be:

$$\tilde{\mathcal{K}}_i(X) = \frac{(1-\nu)\left[(3-4\nu)\sinh(2\mathcal{T}X) - 2\mathcal{T}X\right]}{\mathcal{T}^3 X \left[(3-4\nu)\cosh(2\mathcal{T}X) + 2(\mathcal{T}X)^2 + 5 - 12\nu + 8\nu^2\right]}. \tag{50}$$

It may also be useful to provide the analytical solution for completely incompressible substrates ($\nu = 0.5$) for scenarios such as AFM measurements on thin gels and tissues. In this context, we find that the kernel function simplifies to

$$\tilde{\mathcal{K}}_i \to X^2/3 \quad \text{as} \quad \mathcal{T} \to 0 \quad \text{and} \quad \nu \to 1/2. \tag{51}$$

and perturbation structure becomes:

$$W_0 + \epsilon_i \left(W_1 - \frac{1}{3}\mathcal{H}_0^{-1}\left[\tilde{P}_0 X^2\right]\right) + \epsilon_i^2 \left(W_2 - \frac{1}{3}\mathcal{H}_0^{-1}\left[\tilde{P}_1 X^2\right]\right) + \cdots = 0$$

$$\left(P_0 - \frac{1}{W_s^3}\right) + \epsilon_i \left(P_1 - \frac{3W_1}{W_s^4}\right) + \epsilon_i^2 \left(P_2 - \frac{6W_1^2}{W_s^5} - \frac{3W_2}{W_s^4}\right) + \cdots = 0. \tag{52}$$

After inverse transform and some algebra, we obtain the first-order solution for the experimentally accessible parameters, including $\mathcal{F} - S$ and $D - S$ relations

$$\mathcal{F} = \frac{\pi}{S^2} + \frac{6\pi}{7S^7}\epsilon_i + O(\epsilon_i^2) \quad \text{and} \quad D = \left(S + \frac{\pi}{S^2}\right) + \frac{6\pi}{7S^7}\epsilon_i + O(\epsilon_i^2) \tag{53}$$

and parameters at jump-to-contact points

$$S_c = (2\pi)^{1/3} + \frac{1}{2 \times 2^{1/3}\pi^{4/3}}\epsilon_i, \quad D_c = \left(\frac{27\pi}{4}\right)^{1/3} + \frac{3}{14 \times 2^{1/3}\pi^{4/3}}\epsilon_i, \quad \mathcal{F}_c = \left(\frac{\pi}{4}\right)^{1/3} - \frac{2^{2/3}}{7\pi^{4/3}}\epsilon_i. \tag{54}$$

The problem can be solved numerically given the effective stiffness $\mathcal{T}$, effective deformability ϵ_i, and the effective compressibility C (or Poisson's ratio v). In Fig. 8a and b, we set $\mathcal{T} = 0.01$ and $v = 1/2$ (i.e., $C = 0$) to illustrate the fold bifurcation structure that has been observed in the case of thin compressible and semi-infinite substrates. As expected, Eq. (53) shows excellent agreement with numerical results for small ϵ_i. However, it is important to note that achieving $C \ll 1$ in thin substrate systems could be very challenging (Chandler and Vella, 2020). For example, the numerically calculated critical cantilever positions for various values of ϵ_i and v are presented as circle markers in Fig. 8d and e for $\mathcal{T} = 0.01$ and $\mathcal{T} = 0.1$, respectively. We find that the data generally agree well with the solution for a thin compressible substrate (dashed curves in Fig. 8d and e). The $D_c - \epsilon_i$ relations collapse onto a v-independent master curve only in moderately slender systems (e.g., $\mathcal{T} = 0.1$) and when v is set very close to 0.5. This can also be explained by Eq. (47), which shows that compressibility is proportional to $\mathcal{T}^{-2}$, making it significantly amplified in thin substrate systems where $\mathcal{T} \ll 1$. For example, when $\mathcal{T} = 0.01$, the effective compressibility remains quite large (~ 10) even at $v = 0.4995$.

4. General vdW interactions

We now turn our attention to retarded van der Waals forces, which, as described by Eq. (9), decay more rapidly than in the non-retarded case. To generalize the conclusion, we instead take

$$p_{\text{vdW}} = B/g^n, \tag{55}$$

where at least $n > 1$ is required to ensure a finite pulling force. This form may be advantageous for characterizing van der Waals interactions between inhomogeneous materials (Hermann et al., 2017).

4.1. Characteristic length scales

The methodology for analyzing the jump-to-contact due to vdW forces in the form of Eq. (55) remains the same as that outlined in the previous section. Therefore, we will not repeat the detailed formulation and calculations. Instead, we will provide a concise overview of the characteristic length scales and the analytical results associated with the premature jump-to-contact caused by retarded vdW forces. Firstly, the characteristic gap and horizontal lengths becomes

$$\bar{s}_* := (BR_s/k)^{1/n} \tag{56}$$

and

$$\bar{\ell}_* := (R_s s_*)^{1/2} = B^{1/2n} R_s^{(n+1)/2n}/k^{1/2n}, \tag{57}$$

respectively. As a consequence, the effective thickness of the substrate is defined by

$$\bar{\mathcal{T}} := \frac{t}{\bar{\ell}_*} = \frac{tk^{1/2n}}{B^{1/2n} R_s^{(n+1)/2n}}. \tag{58}$$

We then discuss the analytical solutions for the critical sphere-substrate gap, cantilever position, and pulling force at the onset of instability, which can be derived in the limits of thin ($\bar{\mathcal{T}} \ll 1$) and thick ($\bar{\mathcal{T}} \gg 1$) substrates

4.2. Thin substrates ($\bar{\mathcal{T}} \ll 1$)

As in the previous section, a thin substrate generally appears quite compressible, as its effective compressibility is

$$\bar{C} := (1 - 2v)\frac{\bar{\ell}_*^2}{t^2} = (1 - 2v)\bar{\mathcal{T}}^{-2}, \tag{59}$$

which is obtained by comparing the first two terms in the expansion of the kernel function in Eq. (13). We thus only focus on the case of thin, compressible substrates, for which the effective deformability can be defined as

$$\bar{\epsilon}_c := \frac{(1 - 2v)tB}{2(1 - v)Gs_*^{n+1}} = \frac{(1 - 2v)tk^{(n+1)/n}}{2(1 - v)GB^{1/n} R_s^{(n+1)/n}}. \tag{60}$$

Under the condition that $\bar{T} \ll 1$, $\bar{C} \gg 1$, and $\bar{\epsilon}_c \ll 1$, we can obtain the following structure:

$$W_0 + \bar{\epsilon}_c(W_1 - P_0) + \cdots = 0, \quad \text{and} \quad \left(P_0 - \frac{1}{W_s^n}\right) + \bar{\epsilon}_c\left(P_1 - \frac{nW_1}{W_s^{n+1}}\right) + \cdots = 0. \tag{61}$$

Solving this at each order of $\bar{\epsilon}_c$ immediately gives the analytical relationships between the separation-displacement ($S - D$) and force–displacement ($\mathcal{F} - D$) in typical AFM measurements:

$$D = \left[S + \frac{2\pi}{(n - 1)S^{n-1}}\right] + \frac{\pi}{S^{2n}}\bar{\epsilon}_c \quad \text{and} \quad \mathcal{F} = \frac{2\pi}{(n - 1)S^{n-1}}\left(1 + \frac{n - 1}{2S^{n+1}}\bar{\epsilon}_c\right). \tag{62}$$

Accordingly, critical conditions of the first-order approximation can be expressed as:

$$S_c = (2\pi)^{1/n} + \frac{1}{2\pi}\bar{\epsilon}_c, \quad D_c = \frac{n(2\pi)^{1/n}}{n - 1} + \frac{1}{4\pi}\bar{\epsilon}_c, \quad \text{and} \quad \mathcal{F}_c = \frac{(2\pi)^{1/n}}{n - 1} - \frac{1}{4\pi}\bar{\epsilon}_c. \tag{63}$$

Interestingly, the dependence of $\bar{\epsilon}_c$ in Eq. (63) is independent of the specific value of n. In addition, we expect these results to provide a reasonable approximation even when $\bar{\epsilon} \sim 1$ and $\bar{\mathcal{T}} \sim 1$, as suggested by the observations in Fig. 6.

4.3. Thick substrates ($\bar{\mathcal{T}} \gg 1$)

For a thick substrate subject to retarded vdW attraction from the sphere, its effective deformability can be defined as

$$\bar{\epsilon}_s := \frac{B\bar{\ell}_*}{Gs_*^{n+1}} = \frac{k^{(2n+1)/2n}}{GB^{1/2n}R_s^{(n+1)/2n}}, \tag{64}$$

which is related to the deformability of thin substrates by $\bar{\epsilon}_c = (1-2\nu)\bar{\mathcal{T}}\bar{\epsilon}_s/[2(1-\nu)]$. When $\bar{\epsilon}_s$ is small, we obtain

$$W_0 + \bar{\epsilon}_s\left\{W_1 - (1-\nu)\mathcal{H}_0^{-1}\left[\tilde{P}_0/|X|\right]\right\} + \cdots = 0 \quad \text{and} \quad \left(P_0 - \frac{1}{W_s^n}\right) + \bar{\epsilon}_s\left(P_1 - \frac{nW_1}{W_s^{n+1}}\right) + \cdots = 0. \tag{65}$$

We solve this problem up to the order of $O(\bar{\epsilon}_s)$ and obtain

$$W_1(\rho) = \frac{(1-\nu)\sqrt{\pi/2}\,\Gamma(n-1/2)\,{}_2F_1\left(\frac{1}{2}, n-\frac{1}{2}, 1, -\frac{\rho^2}{2S}\right)}{\Gamma(n)\,S^{n-1/2}} \tag{66}$$

and

$$P_1(\rho) = \frac{(1-\nu)\sqrt{\pi/2}\,n\,\Gamma(n-1/2)\,{}_2F_1\left(\frac{1}{2}, n-\frac{1}{2}, 1, -\frac{\rho^2}{2S}\right)}{\Gamma(n)\,S^{n-1/2}\left(S+\rho^2/2\right)^{n+1}} \tag{67}$$

where ${}_2F_1$ is the hypergeometric function, and Γ is the Euler gamma function (Abramowitz and Stegun, 1968). We can draw straightforward conclusions when $n = (2+N)/2$ (where N is an positive integer):

$$D = \left[S + \frac{2\pi}{(n-1)S^{n-1}}\right] + \frac{\alpha(n)(1-\nu)\pi^3}{\sqrt{2}S^{(4n-1)/2}}\bar{\epsilon}_s \quad \text{and} \quad \mathcal{F} = \frac{2\pi}{(n-1)S^{n-1}} + \frac{\alpha(n)(1-\nu)\pi^3}{\sqrt{2}S^{(4n-1)/2}}\bar{\epsilon}_s, \tag{68}$$

where $\alpha(n) \approx 0.53\exp(-n/0.96) + 0.16\exp(-n/5.41) + 0.059$ with an error of less than 1% for $2 \leq n \leq 10$. We then obtain the critical jump-to-contact parameters, including:

$$S_c \approx (2\pi)^{1/n} + \frac{\alpha(n)(4n-1)\pi^{(2n+1)/2n}}{n\,2^{(7n-1)/2n}}(1-\nu)\bar{\epsilon}_s \tag{69}$$

and

$$D_c \approx \frac{n(2\pi)^{1/n}}{n-1} + \frac{\alpha(n)\pi^{(2n+1)/2n}}{2^{(5n-1)/2n}}(1-\nu)\bar{\epsilon}_s, \quad \mathcal{F}_c \approx \frac{(2\pi)^{1/n}}{n-1} - \frac{\alpha(n)(2n-1)\pi^{(2n+1)/2n}}{n\,2^{(7n-1)/2n}}(1-\nu)\bar{\epsilon}_s. \tag{70}$$

Unlike the n independence observed in thin substrates, the coefficients of the $\bar{\epsilon}_s$ in Eqs. (69) and (70) decrease by more than a factor of 3 as n increases from 2 to 10.

5. Conclusions

We have investigated the jump-to-contact phenomenon on a deformable substrate that has been commonly observed in AFM measurements. Our findings revealed that the deformability of the substrate can cause this phenomenon to occur prematurely, (i.e. occurring at a greater sphere-substrate separation or a farther position of the cantilever holder). Using perturbation theory, we have made analytical progress for this premature jump-to-contact, which may facilitate precise measurements of the strength and retardation effects of van der Waals forces in soft materials and structures that are increasingly important. For example, recent experiments have indicated a strong signature of the many-body nature of van der Waals interactions in complex materials, which remains far from well-characterized (see a relevant review by Hermann et al., 2017). To better elucidate these many-body effects, it is necessary to perform van der Waals force measurements on materials of extreme thinness and thus high deformability, which could be achieved by exploiting the critical jump forces and distances in premature jump-to-contact instability.

Although discussed within the framework of linearly elastic substrates, the concept presented here can be readily extended to other linear systems, such as liquid surfaces, soap films, suspended nanoflakes, tensed membranes and sheets, and elastic shells, of which the deformability is intrinsically high. In these cases, the physical boundary of the surface becomes significant, particularly when the contact point is close to it. Alternatively, measuring the jump-to-contact across the entire sample surface might provide opportunities for the determination of additional mechanical and surface parameters, such as residual stress, which are challenging to measure using other experimental techniques. However, for highly deformable structures, it is likely to reach a nonlinear deformation region where no Green's function exists to describe their mechanical response to van der Waals attraction, the elasticity bit in the model described in Section 2 is not applicable but should be readily modified to account for material and geometrical nonlinearities.

The relatively simple framework of our theory has enabled the exploration of some key features of the jump-to-contact phenomenon in deformable systems. However, our analysis overlooks several important practical aspects of AFM measurements. In particular, contact between the AFM tip and the surface is often mediated by a liquid of a certain viscosity. As a result, dynamics become significant: i) The liquid medium can generate shear stresses on the sample surface, leading to additional deformation (Rallabandi, 2024). (ii) The onset of fold bifurcation will sensitively depend on the proximity to the bifurcation point and the speed at which the sphere approaches or passes the bifurcation point (Gomez et al., 2017). (iii) The interplay between attractive van der Waals forces and repulsive elastohydrodynamic lifting forces introduces a good deal of complexities into the mechanics of the jump-to-contact (if still any) (Roberts, 1971). These factors are not considered in this work.

CRediT authorship contribution statement

Chuanli Yu: Writing – original draft, Validation, Investigation. **Zhaohe Dai:** Writing – review & editing, Writing – original draft, Investigation, Formal analysis, Conceptualization.

Declaration of competing interest

The authors declare that they have no known competing financial interests or personal relationships that could have appeared to influence the work reported in this paper.

Acknowledgments

Data availability

Data will be made available on request.

References

Abramowitz, M., Stegun, I.A., 1968. Handbook of Mathematical Functions with Formulas, Graphs, and Mathematical Tables. vol. 55, US Government printing office.

Bertin, V., Amarouchene, Y., Raphaël, E., Salez, T., 2022. Soft-lubrication interactions between a rigid sphere and an elastic wall. J. Fluid Mech. 933, A23.

Bradley, R.S., 1932. LXXIX. The cohesive force between solid surfaces and the surface energy of solids. Lond. Edinb. Dublin Philosoph. Mag. J. Sci. 13 (86), 853–862.

Butt, H.J., Cappella, B., Kappl, M., 2005. Force measurements with the atomic force microscope: Technique, interpretation and applications. Surf. Sci. Rep. 59 (1–6), 1–152.

Casimir, H.B., 1948. On the attraction between two perfectly conducting plates. In: Proc. Kon. Ned. Akad. Wet.. vol. 51, p. 793.

Casimir, H.B., Polder, D., 1948. The influence of retardation on the London-van der Waals forces. Phys. Rev. 73 (4), 360.

Chandler, T.G., Vella, D., 2020. Validity of Winkler's mattress model for thin elastomeric layers: beyond Poisson's ratio. Proc. R. Soc. A 476 (2242), 20200551.

Ciavarella, M., Greenwood, J., Barber, J., 2017. Effect of tabor parameter on hysteresis losses during adhesive contact. J. Mech. Phys. Solids 98, 236–244.

Ciavarella, M., Joe, J., Papangelo, A., Barber, J., 2019. The role of adhesion in contact mechanics. J. R. Soc. Interface 16 (151), 20180738.

Costa, L., Li-Destri, G., Pontoni, D., Konovalov, O., Thomson, N.H., 2017. Liquid–liquid interfacial imaging using atomic force microscopy. Adv. Mater. Interfaces 4 (16), 1700203.

Dai, Z., Liu, L., Zhang, Z., 2019. Strain engineering of 2D materials: issues and opportunities at the interface. Adv. Mater. 31 (45), 1805417.

Dai, Z., Lu, N., 2021. Poking and bulging of suspended thin sheets: Slippage, instabilities, and metrology. J. Mech. Phys. Solids 149, 104320.

Dai, Z., Lu, N., Liechti, K.M., Huang, R., 2020. Mechanics at the interfaces of 2D materials: Challenges and opportunities. Curr. Opin. Solid State Mater. Sci. 24 (4), 100837.

Dai, Z., Vella, D., 2022. Droplets on lubricated surfaces: The slow dynamics of skirt formation. Phys. Rev. Fluids 7 (5), 054003.

Derjaguin, B., 1934. Untersuchungen ueber die reibung und adhaesion, IV: Theorie des anhaftens kleiner teilchen. Kolloid-Zeitschrift 69, 155–164.

Derjaguin, B., Abrikosova, I., Lifshitz, E., 1956. Direct measurement of molecular attraction between solids separated by a narrow gap. Q. Rev. Chem. Soc. 10 (3), 295–329.

Dillard, D.A., Mukherjee, B., Karnal, P., Batra, R.C., Frechette, J., 2018. A review of Winkler's foundation and its profound influence on adhesion and soft matter applications. Soft Matter 14 (19), 3669–3683.

Fang, Z., Dai, Z., Wang, B., Tian, Z., Yu, C., Chen, Q., Wei, X., 2022. Pull-to-peel of two-dimensional materials for the simultaneous determination of elasticity and adhesion. Nano Lett. 23 (2), 742–749.

Feng, J.Q., 2000. Contact behavior of spherical elastic particles: a computational study of particle adhesion and deformations. Colloids Surf. A 172 (1–3), 175–198.

Feynman, R., 1959. There's plenty of room at the bottom. https://www.zyvex.com/nanotech/feynman.html.

French, R.H., Parsegian, V.A., Podgornik, R., Rajter, R.F., Jagota, A., Luo, J., Asthagiri, D., Chaudhury, M.K., Chiang, Y.m., Granick, S., et al., 2010. Long range interactions in nanoscale science. Rev. Modern Phys. 82 (2), 1887–1944.

Garcıa, R., Perez, R., 2002. Dynamic atomic force microscopy methods. Surf. Sci. Rep. 47 (6–8), 197–301.

Gomez, M., Moulton, D.E., Vella, D., 2017. Critical slowing down in purely elastic 'snap-through'instabilities. Nat. Phys. 13 (2), 142–145.

Greenwood, J., 1997. Adhesion of elastic spheres. Proc. R. Soc. Lond. Ser. A Math. Phys. Eng. Sci. 453 (1961), 1277–1297.

Guimarães, C.F., Gasperini, L., Marques, A.P., Reis, R.L., 2020. The stiffness of living tissues and its implications for tissue engineering. Nat. Rev. Mater. 5 (5), 351–370.

Hamaker, H.C., 1937. The London—van der Waals attraction between spherical particles. Physica 4 (10), 1058–1072.

Hannah, M., 1951. Contact stress and deformation in a thin elastic layer. Quart. J. Mech. Appl. Math. 4 (1), 94–105.

Hermann, J., DiStasio, Jr., R.A., Tkatchenko, A., 2017. First-principles models for van der Waals interactions in molecules and materials: Concepts, theory, and applications. Chem. Rev. 117 (6), 4714–4758.

Israelachvili, J.N., 2011. Intermolecular and Surface Forces. Academic Press.

Israelachvili, J.N., Tabor, D., 1972. The measurement of van der waals dispersion forces in the range 1.5 to 130 nm. Proc. R. Soc. A 331 (1584), 19–38.

Jones, J.E., 1924. On the determination of molecular fields.—II. From the equation of state of a gas. Proc. R. Soc. Lond. Ser. Contain. Pap. Math. Phys. Character 106 (738), 463–477.

Krieg, M., Fläschner, G., Alsteens, D., Gaub, B.M., Roos, W.H., Wuite, G.J., Gaub, H.E., Gerber, C., Dufrêne, Y.F., Müller, D.J., 2019. Atomic force microscopy-based mechanobiology. Nat. Rev. Phys. 1 (1), 41–57.

Li, J., Zhang, G., Wang, L., Dai, Z., 2024. Indentation of a plate on a thin transversely isotropic elastic layer. Acta Mech. Solida Sin. http://dx.doi.org/10.1007/s10338-024-00532-1.

Lifshitz, E.M., 1956. The theory of molecular attractive forces between solids. vol. 2, Elsevier, pp. 73–83,

Liu, M., Gomez, M., Vella, D., 2021. Delayed bifurcation in elastic snap-through instabilities. J. Mech. Phys. Solids 151, 104386.

London, F., 1937. The general theory of molecular forces. Trans. Faraday Soc. 33, 8b–26.

Maugis, D., 2013. Contact, Adhesion and Rupture of Elastic Solids. vol. 130, Springer Science & Business Media.

Polyanin, A.D., 2001. Handbook of Linear Partial Differential Equations for Engineers and Scientists. Chapman and hall/crc.

Rallabandi, B., 2024. Fluid-elastic interactions near contact at low reynolds number. Annu. Rev. Fluid Mech. 56 (1), 491–519.

Rao, Y., Lu, N., 2024. Effects of adhesive and frictional contacts on the nanoindentation of two-dimensional material drumheads. J. Mech. Phys. Solids 105828.

Roberts, A., 1971. Squeeze films between rubber and glass. J. Phys. D: Appl. Phys. 4 (3), 423.

Rouweler, G., Overbeek, J.T.G., 1971. Dispersion forces between fused silica objects at distances between 25 and 350 nm. Trans. Faraday Soc. 67, 2117–2121.

Rutland, M.W., Tyrrell, J.W., Attard, P., 2004. Analysis of atomic force microscopy data for deformable materials. J. Adhes. Sci. Technol. 18 (10), 1199–1215.

Sneddon, I.N., 1995. Fourier Transforms. Courier Corporation.

Style, R.W., Dufresne, E.R., 2012. Static wetting on deformable substrates, from liquids to soft solids. Soft Matter 8 (27), 7177–7184.

Tabor, D., Winterton, R.S., 1969. The direct measurement of normal and retarded van der Waals forces. Proc. R. Soc. A 312 (1511), 435–450.

Tang, L., Wang, M., Ng, C., Nikolic, M., Chan, C.T., Rodriguez, A.W., Chan, H.B., 2017. Measurement of non-monotonic Casimir forces between silicon nanostructures. Nat. Photonics 11 (2), 97–101.

Tavakol, B., Froehlicher, G., Holmes, D.P., Stone, H.A., 2017. Extended lubrication theory: improved estimates of flow in channels with variable geometry. Proc. R. Soc. Lond. Ser. A Math. Phys. Eng. Sci. 473 (2206), 20170234.

Tomlinson, G., 1928. LXVII. Molecular cohesion. Lond. Edinb. Dublin Philosop. Mag. J. Sci. 6 (37), 695–712.

Wang, G., Dai, Z., Xiao, J., Feng, S., Weng, C., Liu, L., Xu, Z., Huang, R., Zhang, Z., 2019. Bending of multilayer van der waals materials. Phys. Rev. Lett. 123 (11), 116101.

Wu, J.J., 2010. The jump-to-contact distance in atomic force microscopy measurement. J. Adhes. 86 (11), 1071–1085.